Synthesis of Lead-Free $Cs_4(Cd_{1-x}Mn_x)Bi_2Cl_{12}$ ($0 \leq x \leq 1$) Layered Double Perovskite Nanocrystals with Controlled Mn-Mn Coupling Interaction

Hanjun Yang, Wenwu Shi, Tong Cai, Katie Hills-Kimball, Zhenyang Liu, Lacie Dube and Ou Chen[*]

Department of Chemistry, Brown University, 324 Brook Street, Providence, Rhode Island 02912, United States

*E-mail: ouchen@brown.edu

Table of Content

1. **Chemicals 3**
2. **Synthesis 3**
3. **Characterizations 3**
4. **Density Functional Theory (DFT) Calculations 5**
5. **Synthesis, Structure, and Optical Properties of the $Cs_4M(II)Bi_2Cl_{12}$ LDP Powder 5**
6. **Supporting Figures and Tables 7**

References 31

1. Chemicals

Cesium carbonate (Cs_2CO_3, 99.9%), bismuth acetate ($Bi(OAc)_3$, >99.99%), manganese chloride ($MnCl_2$, >99%), cadmium chloride ($CdCl_2$, >99.99% trace metal basis), 1-octadecene (ODE, technical grade, 90%), oleylamine (OAm, technical grade, 70%) , oleic acid (OA, technical grade, 90%) and nitric acid (70%, ≥99.999% trace metals basis) were purchased from Aldrich. Benzoyl chloride (99+%), cadmium acetate dihydrate ($Cd(OAc)_2 \cdot 2H_2O$, 99.999%) and cesium chloride (CsCl, 99.99% metal basis) were obtained from Alfa Aesar. Manganese acetate tetrahydrate ($Mn(OAc)_2 \cdot 4H_2O$, 99.999%) and bismuth oxide (Bi_2O_3, 99.9%) were obtained from ACROS. Hydrochloric acid (37%, ACS plus), hexane, toluene and isopropanol were obtained from Fisher. All chemicals were used as received without further purification.

2. Synthesis

Synthesis of $Cs_4M(II)Bi_2Cl_{12}$ (M(II) = Cd, Mn) layered double perovskite (LDP) nanocrystals (NCs)

The synthesis of $Cs_4M(II)Bi_2Cl_{12}$ NCs was based on a modified hot-injection synthesis method.[1] Cs_2CO_3 (40 mg, 0.12 mmol), $Bi(OAc)_3$ (100 mg, 0.26 mmol) and metal acetate ($Cd(OAc)_2 \cdot 2H_2O$ (69.0 mg, 0.26 mmol) or $Mn(OAc)_2 \cdot 4H_2O$ (63.5 mg, 0.26 mmol)) were mixed in ODE (10 mL). OA(1.5 mL) and OAm (0.5 mL) were added to the ODE solution. The mixture was heated to 70 °C under vacuum to remove water and oxygen for 1 hour, then heated at 100 °C for an additional 30 minutes. The mixture was then heated in nitrogen atmosphere to 170 °C. Upon reaching 170 °C, benzoyl chloride (0.4 mL, 3.4 mmol, mixed with 0.4 mL ODE) was swiftly injected into the solution, which initiated the nucleation and growth of NCs. The mixture was allowed to react at 170 °C for 30 seconds, before being cooled down to room temperature in an ice-water bath. The NCs were separated from ODE by adding isopropanol, then centrifuged at 8000 rpm for 10 minutes. The precipitate that contained the NCs was then redispersed in toluene. For $Cs_4(Cd_{1-x}Mn_x)Bi_2Cl_{12}$ NCs, a mixture of $Cd(OAc)_2 \cdot 2H_2O$ and $Mn(OAc)_2 \cdot 4H_2O$ with different molar ratios were used as precursors and the rest of the synthesis in unchanged.

Synthesis of $Cs_4M(II)Bi_2Cl_{12}$ (M(II) = Cd, Mn) powders

The synthesis of $Cs_4M(II)Bi_2Cl_{12}$ powder was adopted from the synthesis of $Cs_4MnSb_2Cl_{12}$ with modifications.[2] Bi_2O_3 (93.2 mg, 0.20 mmol), metal chloride ($CdCl_2$ (36.7 mg, 0.20 mmol) or $MnCl_2$ (25.2 mg, 0.20 mmol)) were dissolved in HCl (1 mL) separately. After complete dissolution, the Bi-containing solution was mixed with the metal chloride solution. CsCl (134.7 mg, 0.80 mmol) was dissolved in HCl (0.5 mL), then added to the mixed precursors under stirring. White, slightly yellow precipitates were formed upon the addition of CsCl. The formed $Cs_4M(II)Bi_2Cl_{12}$ powder was centrifuged and washed with 2% HCl once, then ethanol once, then two times with hexane. The wet powders were dried at 70°C for 1 hour, then stored at ambient condition. For the synthesis of $Cs_4(Cd_{1-x}Mn_x)Bi_2Cl_{12}$, a designed amount of $CdCl_2$ and $MnCl_2$ (with different molar ratios) mixture solution was added to the Bi- solution and the rest of the synthesis is unchanged.

3. Characterizations

X-ray diffraction (XRD) measurements

Powder XRD patterns were obtained on a Bruker D8 Discovery 2D X-ray Diffractometer equipped with a Vantec 500 2D area detector working on Cu Kα radiation. NC samples dispersed in toluene were drop-cast on a glass slide under gentle heating to evaporate the solvent. A least-square refinement program UnitCell is used to retrieve lattice constants from the measured XRD patterns.[3] The crystalline domain size is calculated using the Scherrer's formula,

$$S = \frac{K\lambda}{\beta cos\theta}$$

where S is the calculated crystalline domain size, K is the shape factor (0.9), λ is the X-ray wavelength (0.154 nm), β is the full-width-at-half-maximum (FWHM) of diffraction peak, and θ is the diffraction peak position.

X-ray photoelectron spectroscopy (XPS) measurements

XPS spectra were measured on a Thermo Scientific KAlpha+ instrument operating on Al Kα=1486.6 eV radiation with a spot size of ~ 200 μm. Samples dispersed in toluene were drop-cast on silicon wafers and allowed to evaporate with gentle heating. All XPS signals were calibrated by setting the adventitious carbon 1s signal to 284.8 eV.

Transmission electron microscopy (TEM) measurements

TEM microscopy was measured using a JEOL-2100F TEM operating at 200kV. Samples were dispersed in toluene and drop-cast on a 300-mesh TEM grid and allowed to dry under ambient conditions.

Ultraviolet-visible (UV-Vis) absorptions spectroscopy measurements of NCs

Absorption spectra were measured on an Agilent Cary 8454 UV-Vis Spectrometer. Samples were dispersed in toluene for measurement.

Photoluminescence (PL), PL excitation (PLE) spectroscopy and PL quantum yield (PL QY) measurements

PL and PLE spectra were measured on an Edinburgh Instruments FS5 Spectrofluorometer. NCs were dispersed in toluene for PL measurements. 330 nm UV light was used for excitation source for all PL measurements. All PLE measurements were monitored at the PL peak wavelength. PL QYs and powder PL, PLE spectra were measured using a built-in integrating sphere on the Edinburgh Instruments FS5 Spectrofluorometer.

Low-temperature PL spectra were measured using a liquid nitrogen dewar with an EPR tube sample holder. NCs were dissolved in toluene in an EPR tube, submerged in the liquid-nitrogen for 10 minutes until the temperature stabilized. A long-pass filter (cutoff wavelength of 380 nm) was used to remove the scattering excitation light.

Time-resolved PL (TR-PL) decay measurements of NCs

The TR-PL decay curves were measured using Edinburgh Instruments FS5 Spectrofluorometer equipped with a 5W microsecond Xenon flashlamp with a repetition rate of 50 Hz. The solution-based samples were dispersed in toluene in a cuvette and excited at 330 nm. Powder samples were measured in the integrating sphere and low-temperature measurements were measured using the liquid nitrogen cryostat. The lifetime decay was fitted with bi-exponential or tri-exponential decay

$$I(t) = \sum_k I_k \exp{(-t/\tau_k)}$$

where $I(t)$ represents the observed PL intensity at the time of t, I_k and τ_k represent the amplitude and lifetime of exponential decay component of k, respectively. Average lifetimes were calculated by the following equation:

$$\tau_{avg} = \frac{\sum_k I_k \tau_k^2}{\sum_k I_k \tau_k}$$

Relative percentage of the decay component of i (P_i) was calculated by the following equation:

$$P_i = \frac{I_i \tau_i}{\sum_k I_k \tau_k}$$

Electron paramagnetic resonance (EPR) spectroscopy measurements

EPR spectra were measured on a Bruker EMX Plus EPR Spectrometer. Measurements were taken at room temperature with a 9.86 GHz X-band microwave frequency. NC samples were dissolved in toluene for the measurement. Powder samples were measured directly in an EPR tube.

Inductively coupled plasma-atomic emission spectroscopy (ICP-AES) measurements

ICP-AES were measured on a Thermo Scientific iCAP 7400 DUO ICP-AES equipped with a Teledyne ASX-560 240 position autosampler. Samples were digested overnight in warm nitric acid, then further diluted in 2% nitric acid.

4. Density Functional Theory (DFT) Calculations

DFT calculations were performed with Vienna ab initio Simulation Package (VASP) code,[4, 5] with the projector augmented wave (PAW) potentials method[6] to describe the electron-ion interaction. The generalized gradient approximation (GGA) in the scheme of Perdew−Burke−Ernzerhof (PBE) was used to describe the exchange and correlation interactions.[7] The band structures and density of states were calculated with Heyd-Scuseria-Ernzerhof (HSE06)[8] hybrid functional plus spin-orbit-coupling (SOC). The splitting parameter (ω) was set to 0.2 and the component of Hartree-Fock (α=0.25) were used to calculate electronic structures. The plane-wave cut-off energy was set to 500 eV, and the Γ-centered k-point meshes with k-spacing of 0.02π Å^{-1} were employed for sampling the Brillouin zone. The lattice parameters and atomic positions were fully relaxed until the force on each atom was smaller than 0.01 eV/Å, and the convergence threshold of energy for the self-consistent was 10^{-6} eV.

As is previously reported, magnetic ordering is crucial to obtain a reasonable band structure for the $Cs_4MnSb_2Cl_{12}$ perovskite.[9] Both $Cs_4MnBi_2Cl_{12}$ and $Cs_4CdBi_2Cl_{12}$ trigonal phase systems were considered under paramagnetic (PM), ferromagnetic (FM), inter- and intra-layer antiferromagnetic (inter-AFM and intra-AFM) ordering, where the total energies per atom were listed in Table S5. For $Cs_4MnBi_2Cl_{12}$, the intra-AFM ordering resulted in the lowest energy and was thus selected for band structure calculation.

The charge density difference was calculated by the following equation:

$$\Delta\rho(r) = \rho_{\text{comp}} - \rho_{\text{Cs}} - \rho_{\text{M}} - \rho_{\text{Bi}} - \rho_{\text{Cl}}$$

where ρ_{comp} is the charge density of $Cs_4M(II)Bi_2Cl_{12}$ compound, ρ_{Cs}, ρ_{M}, ρ_{Bi} and ρ_{Cl} are the charge densities of Cs^+, M^{2+}, Bi^{3+} and Cl^- ions isolated in $Cs_4M(II)Bi_2Cl_{12}$ perovskite crystal, respectively. The cyan and yellow areas represent the charge depletion and charge accumulation, respectively.

Electronic localization function (ELF) has been proposed based on the second-order Taylor expansion of the spherically averaged pair density.[10] The ELF can be directly applied to visualize bond characters between the ions.[11, 12] A close-to-zero ELF value suggests that the metal-chlorine ionic bonds exist with a very low electron density between the metal and chloride ions.

5. Synthesis, Structure, Optical Properties and Discussions of the $Cs_4M(II)Bi_2Cl_{12}$ LDP Powders

The $Cs_4M(II)Bi_2Cl_{12}$ (M(II) = Cd, Mn) and cationic alloyed $Cs_4(Cd_{1-x}Mn_x)Bi_2Cl_{12}$ powders were synthesized by a metathesis reaction as described in the previous synthesis session. XRD measurements showed that the powder samples possess a layered double perovskite (LDP) crystal structure (Figure S12), further confirmed by the Rietveld fitting result (Figure S13, Table S10-S12). A continuous shift to smaller lattice constant (larger 2θ position) with increasing Mn concentration is observed in the alloyed samples (Figure S12b), thus confirming the formation of complete alloy between Cd and Mn.[13] ICP-AES characterization confirmed a near 1:2 atomic ratio or M(II):Bi, consistent with the stoichiometry of LDP (Table S13).

The PL properties of $Cs_4M(II)Bi_2Cl_{12}$ powders are shown in Figure S14. All Mn-containing samples show characteristic Mn-based orange PL 600-605 nm, while no emission is observed for the $Cs_4CdBi_2Cl_{12}$ sample (Figure S14a). Unlike the absorption/PLE spectra of LDP NCs, the PLE spectra of the powder samples showed strong peaks around 350 nm, in addition to several less intense peaks around 430 nm and 520 nm. The weak PLE peaks are similar to the absorption spectrum of isolated Mn^{2+} ions in solution,[14] and are thus tentatively assigned to the direct excitation of Mn^{2+}. A similar discrepancy between bulk and NC PLE spectra have been reported very recently, which is attributed to a size-dependent effect of the NCs.[15] $Cs_4MnBi_2Cl_{12}$ powder has a low PL QY of 1.2%, while the alloyed samples show enhanced PL QYs, with the maximum value of 46.1% for the [Mn] = 22.7% sample in our measurements (Figure S14c). Similarly, the PL lifetime of $Cs_4(Cd_{1-x}Mn_x)Bi_2Cl_{12}$ powder decreases with increasing Mn concentration (Figure S14b). Given the similarity of optical properties between $Cs_4(Cd_{1-x}Mn_x)Bi_2Cl_{12}$ NC and powder samples (**Figure 4a-e**), we hypothesize that the optical processes in the NCs and powders have similar mechanisms, and are thus omitted here. The existence of a magnetic Mn-Mn coupling in powder samples are confirmed by EPR measurements (Figure S15). The EPR peaks of the powder samples are significantly broadened compared with NC samples, even at very low Mn concentration, which may originate from the anisotropic powder orientations during EPR measurements. With increasing Mn concentration, the EPR peaks gradually become more narrower, which is attributed to the spin-narrowing effect of Mn showing strong Mn-Mn interaction at high concentration.[16, 17]

6. Supporting Figures and Tables

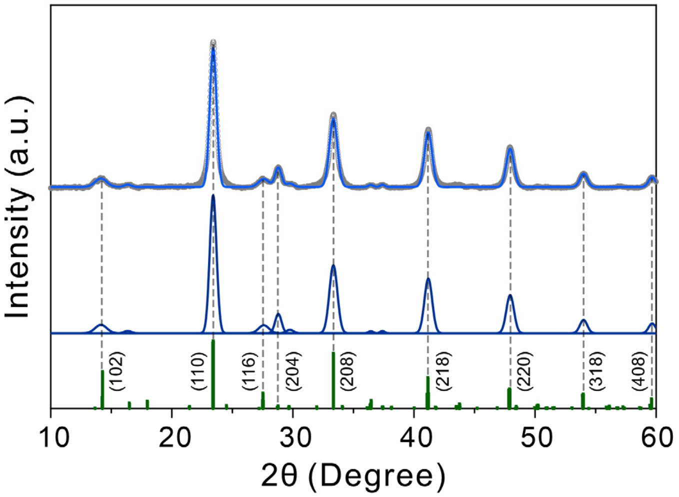

Figure S1. XRD pattern of the $Cs_4CdBi_2Cl_{12}$ LDP NCs. The measured pattern, fitted curves and fitted individual peaks are shown in grey circle, blue line and dark-blue line, respectively. Calculated diffraction peak positions based on the fitting result are marked in green bars. The Miller indices (hkl) of some strong diffraction peaks are labeled.

Table S1. Fitting result of the XRD pattern of the $Cd_4CdBi_2Cl_{12}$ LDP NCs.

Peak number	Miller indices	2θ (º)	FWHM (º)	*d*-spacing (Å)	Crystallite size (nm)
1	(102)	14.14	1.14	6.262	7.0
2	(110)	23.41	0.66	3.800	12.3
3	(116)	27.59	1.00	3.233	8.2
4	(204)	28.80	0.62	3.101	13.2
5	(208)	33.34	0.78	2.688	10.6
6	(218)	41.18	0.75	2.192	11.3
7	(220)	47.94	0.74	1.898	11.7
8	(318)	54.01	0.72	1.698	12.4
9	(408)	59.67	0.68	1.550	13.5

Lattice parameter: $a = 7.574 \pm 0.0003$ Å, $c = 37.36 \pm 0.01$ Å, unit cell volume: 1856.0 ± 0.5 Å^3
Average crystallite size: 11.1 ± 2.2 nm

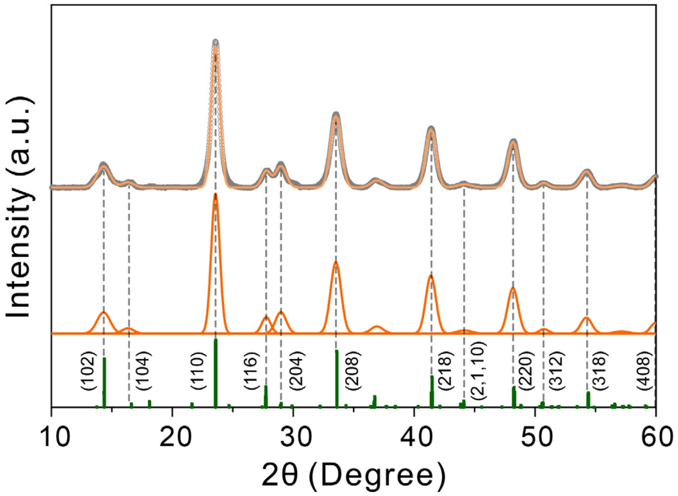

Figure S2. XRD pattern of the $Cs_4MnBi_2Cl_{12}$ LDP NCs. The measured pattern, fitted curves and fitted individual peaks are shown in grey circle, light-orange line and orange line, respectively. Calculated diffraction peak positions based on the fitting result are marked in green bars. The Miller indices (hkl) of some strong diffraction peaks are labeled.

Table S2. Fitting result of the XRD pattern of the $Cd_4MnBi_2Cl_{12}$ NCs.

Peak number	Miller indices	2θ (°)	FWHM (°)	*d*-spacing (Å)	Crystallite size (nm)
1	(102)	14.31	1.27	6.190	6.3
2	(104)	16.33	1.14	5.429	7.1
3	(110)	23.57	0.82	3.774	9.8
4	(116)	27.76	0.87	3.214	9.4
5	(204)	28.98	1.04	3.081	7.9
6	(208)	33.52	1.03	2.673	8.1
7	(218)	41.38	0.98	2.182	8.6
8	(2,1,10)	44.16	1.40	2.051	6.1
9	(220)	48.16	1.00	1.889	8.7
10	(312)	50.73	0.87	1.800	10.1
11	(318)	54.23	1.06	1.691	8.4
12	(408)	59.96	0.96	1.543	9.6

Lattice parameter: $a = 7.542 \pm 0.0003$ Å, $c = 37.16 \pm 0.009$ Å, unit cell volume: 1830.4 ± 0.4 Å^3
Average crystallite size: 8.5 ± 1.2 nm

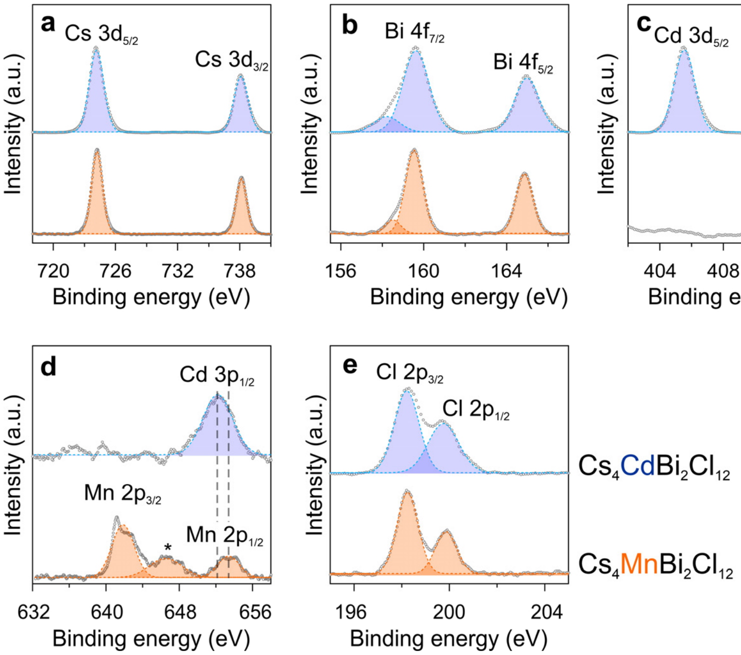

Figure S3. XPS spectra of $Cs_4CdBi_2Cl_{12}$ (blue) and $Cs_4MnBi_2Cl_{12}$ (orange) LDP NCs for Cs 3d **(a)**, Bi 4f **(b)**, Cd 3d **(c)**, Mn 2p **(d)**, and Cl 2p **(e)**. Shaded area marks the gaussian fitting of the XPS peaks. A satellite peak of Mn(II) is marked with an asterisk in (d).[18]

Table S3. ICP-AES-determined Bi, Mn and Cd atomic percentages of $Cs_4(Cd_{1-x}Mn_x)Bi_2Cl_{12}$ LDP NCs.

NC Composition	**Bi (wt. ppm)**	**Mn (wt. ppm)**	**Cd (wt. ppm)**	**(Mn+Cd)/Bi (atom %)**	**Mn/(Mn+Cd) (atom %)**
$Cs_4CdBi_2Cl_{12}$	2.827	0	0.973	64.0	0
$Cs_4(Cd_{0.98}Mn_{0.02})Bi_2Cl_{12}$	3.313	0.007	0.820	46.8	1.7
$Cs_4(Cd_{0.90}Mn_{0.10})Bi_2Cl_{12}$	2.214	0.026	0.470	43.9	10.1
$Cs_4(Cd_{0.65}Mn_{0.35})Bi_2Cl_{12}$	2.444	0.111	0.422	49.3	34.9
$Cs_4(Cd_{0.31}Mn_{0.69})Bi_2Cl_{12}$	2.737	0.264	0.242	53.1	69.0
$Cs_4MnBi_2Cl_{12}$	2.227	0.256	0	43.7	100

Table S4. TR-PL lifetime fitting results of the $Cs_4(Cd_{1-x}Mn_x)Bi_2Cl_{12}$ LDP NCs

NC Composition	**τ (μs)**	**Rel. percentage (%)**	**τ_{avg} (μs)**
$Cs_4(Cd_{0.98}Mn_{0.02})Bi_2Cl_{12}$	41	12	4.4×10^2
	2.5×10^2	48	
	7.9×10^2	41	
$Cs_4(Cd_{0.90}Mn_{0.10})Bi_2Cl_{12}$	41	14	5.6×10^2
	2.7×10^2	44	
	1.1×10^3	41	
$Cs_4(Cd_{0.65}Mn_{0.35})Bi_2Cl_{12}$	36	9.9	3.0×10^2
	1.7×10^2	47	
	5.2×10^2	43	
$Cs_4(Cd_{0.31}Mn_{0.69})Bi_2Cl_{12}$	5.3	21	2.2×10^2
	36	22	
	3.7×10^2	57	
$Cs_4MnBi_2Cl_{12}$	3.4	30	10.1
	13	70	

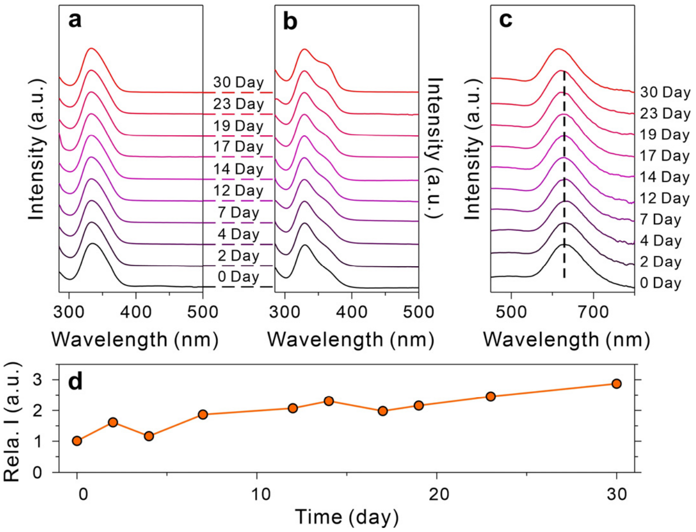

Figure S4. (a, b) The normalized absorption spectra of $Cs_4CdBi_2Cl_{12}$ LDP NCs (a) and $Cs_4MnBi_2Cl_{12}$ LDP NCs (b) upon storage. **(c)** The normalized PL spectra of $Cs_4MnBi_2Cl_{12}$ LDP NCs. **(d)** The relative intensity (Rela. I) of PL spectra of $Cs_4MnBi_2Cl_{12}$ LDP NCs collected at different storage times.

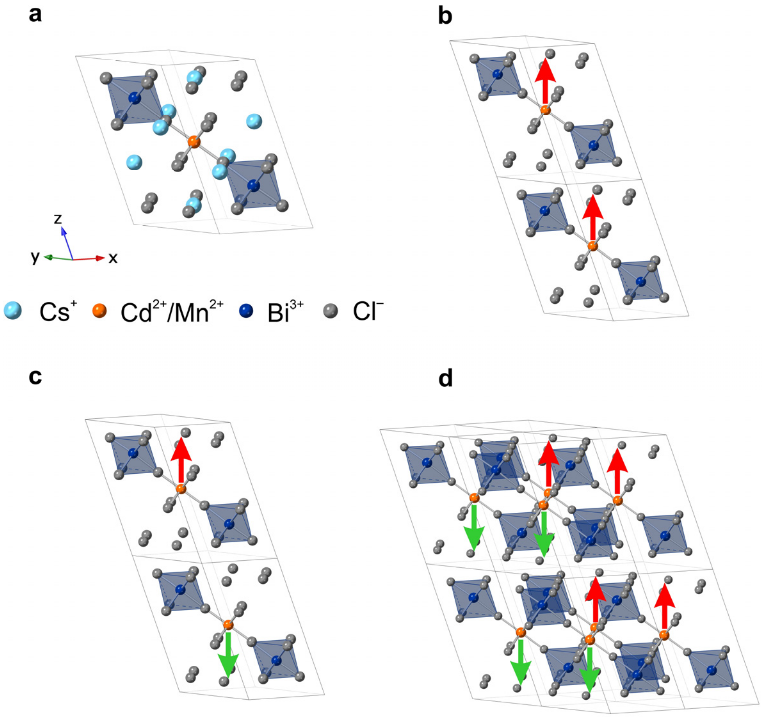

Figure S5. Schematic illustration of the crystal structure of **(a)** Primitive cell of $Cs_4M(II)Bi_2Cl_{12}$ LDP. **(b-d)** Ferromagnetic (b), inter-layer AFM (c), and intra-layer AFM (d) models used to address the magnetic structure of $Cs_4MnBi_2Cl_{12}$. Red and green arrows next to the Mn atoms represent the spin-up and spin-down state of Mn centers respectively. Cs atoms are omitted for clarity in (b-d).

Table S5. Calculated total energy per atom of different magnetic models for $Cs_4MnBi_2Cl_{12}$.

Composition	**PM (eV)**	**FM (eV)**	**Inter-AFM (eV)**	**Intra-AFM (eV)**
$Cs_4MnBi_2Cl_{12}$	-3.636	-3.694	-3.721	-3.722

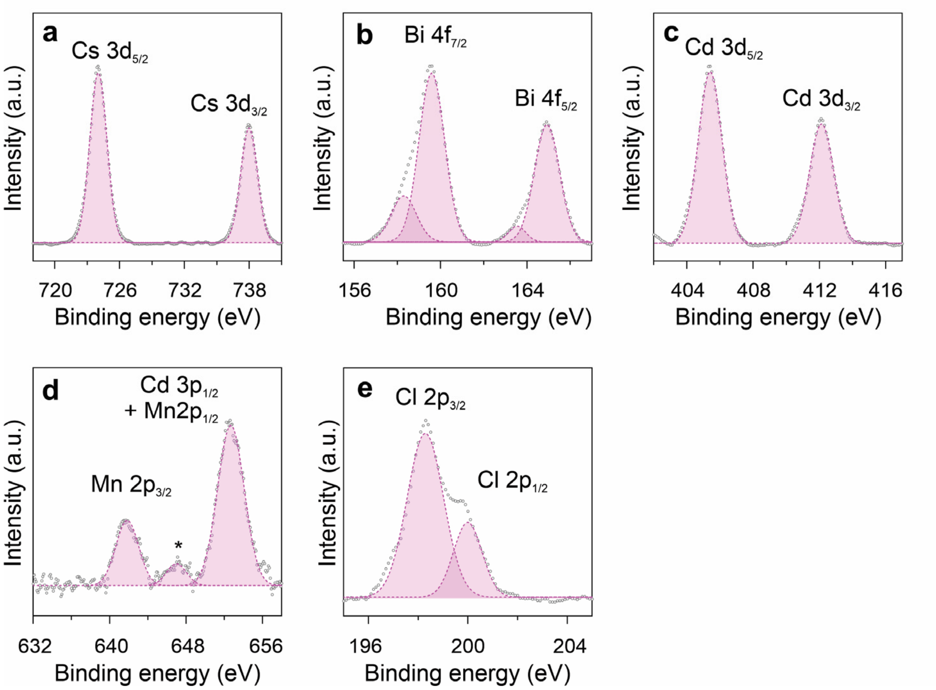

Figure S6. XPS spectra of $Cs_4(Cd_{1-x}Mn_x)Bi_2Cl_{12}$ (x = 34.9%) LDP NCs for Cs 3d **(a)**, Bi 4f **(b)**, Cd 3d **(c)**, Mn 2p **(d)**, and Cl 2p **(e)**. Shaded area marks the gaussian fitting of the XPS signal. A satellite peak of Mn is marked with an asterisk in (d).

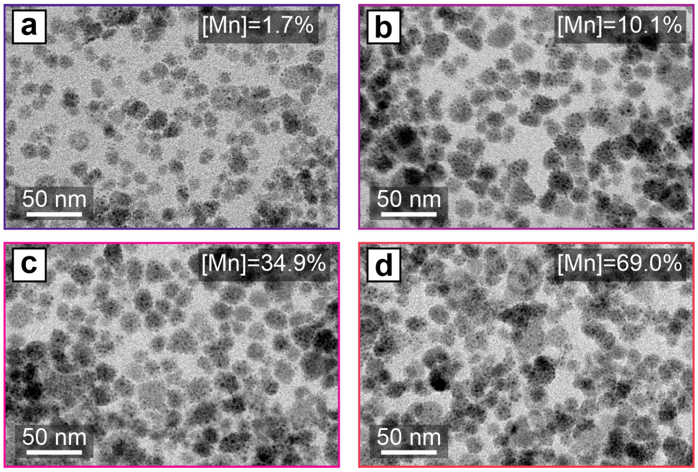

Figure S7. (a-d) TEM images of $Cs_4(Cd_{1-x}Mn_x)Bi_2Cl_{12}$ LDP NCs, x = 1.7% (a), x = 10.1% (b), x = 34.9% (c) and x = 69.0% (d).

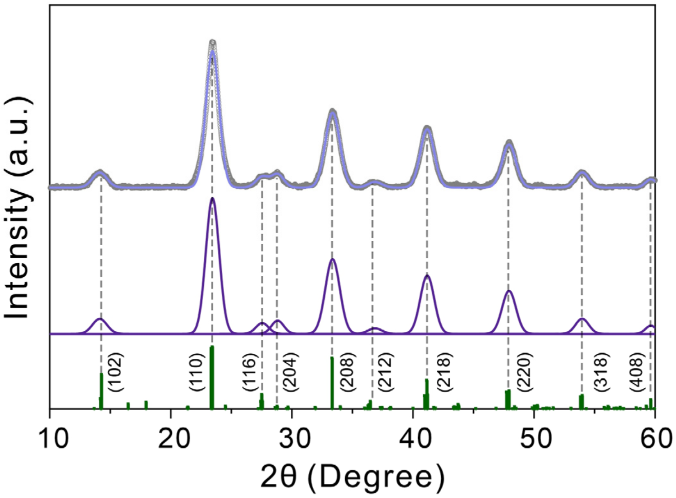

Figure S8. XRD pattern of the $Cs_4(Cd_{0.98}Mn_{0.02})Bi_2Cl_{12}$ LDP NCs. The measured pattern, fitted curves and fitted individual peaks are shown in grey circle, light-purple line and purple line, respectively. Calculated diffraction peak positions based on the fitting result are marked in green bars. The Miller indices (hkl) of some strong diffraction peaks are labeled.

Table S6. Fitting result of the XRD pattern of the $Cs_4(Cd_{0.98}Mn_{0.02})Bi_2Cl_{12}$ LDP NCs.

Peak number	**Miller indices**	**2θ (°)**	**FWHM (°)**	***d*-spacing (Å)**	**Crystallite size (nm)**
1	(102)	14.13	1.41	6.270	5.7
2	(110)	23.44	1.30	3.795	6.3
3	(116)	27.55	1.24	3.238	6.6
4	(204)	28.82	1.20	3.098	6.9
5	(208)	33.36	1.41	2.686	5.9
6	(212)	36.86	1.34	2.439	6.3
7	(218)	41.18	1.35	2.192	6.3
8	(220)	47.93	1.35	1.898	6.4
9	(318)	53.97	1.29	1.699	6.9
10	(408)	59.65	1.06	1.550	8.6

Lattice parameter: $a = 7.582 \pm 0.0004$ Å, $c = 37.37 \pm 0.01$ Å, unit cell volume: 1860.5 ± 0.5 Å^3
Average crystallite size: 6.6 ± 0.8 nm

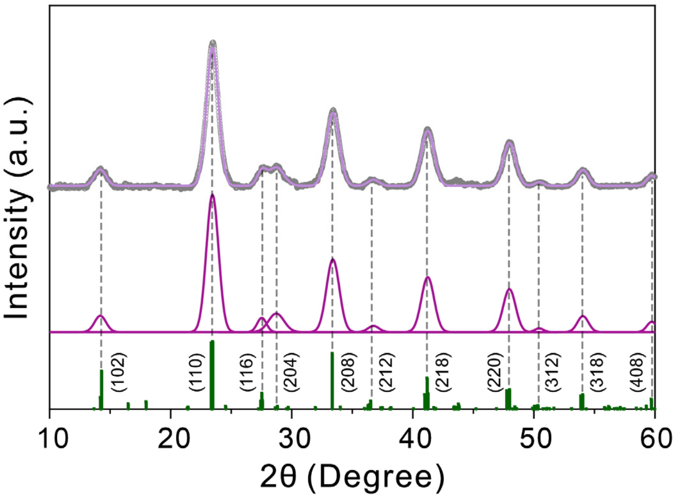

Figure S9. XRD pattern of the $Cs_4(Cd_{0.90}Mn_{0.10})Bi_2Cl_{12}$ LDP NCs. The measured pattern, fitted curves and fitted individual peaks are shown in grey circle, light-purple line and purple line, respectively. Calculated diffraction peak positions based on the fitting result are marked in green bars. The Miller indices (hkl) of some strong diffraction peaks are labeled.

Table S7. Fitting result of the XRD pattern of the $Cs_4(Cd_{0.90}Mn_{0.10})Bi_2Cl_{12}$ LDP NCs.

Peak number	**Miller indices**	**2θ (°)**	**FWHM (°)**	***d*-spacing (Å)**	**Crystallite size (nm)**
1	(102)	14.19	1.12	6.244	7.2
2	(110)	23.45	1.18	3.794	6.9
3	(116)	27.53	0.89	3.241	9.1
4	(204)	28.72	1.50	3.108	5.5
5	(208)	33.40	1.25	2.683	6.6
6	(212)	36.75	1.07	2.446	7.8
7	(218)	41.23	1.24	2.190	6.9
8	(220)	47.98	1.20	1.896	7.2
9	(312)	50.44	0.84	1.810	10.4
10	(318)	54.05	1.08	1.697	8.3
11	(408)	59.73	0.95	1.548	9.7

Lattice parameter: $a = 7.586 \pm 0.0004$ Å, $c = 37.25 \pm 0.01$ Å, unit cell volume: 1856.4 ± 0.5 Å^3
Average crystallite size: 7.8 ± 1.5 nm

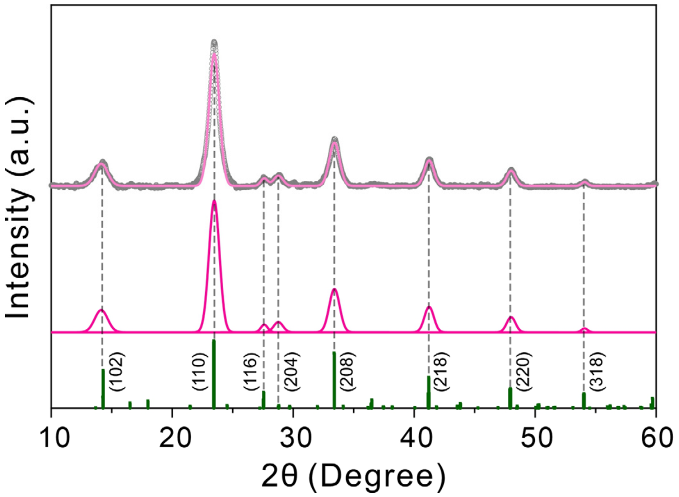

Figure S10. XRD pattern of the $Cs_4(Cd_{0.65}Mn_{0.35})Bi_2Cl_{12}$ LDP NCs. The measured pattern, fitted curves and fitted individual peaks are shown in grey circle, pink line and magenta line, respectively. Calculated diffraction peak positions based on the fitting result are marked in green bars. The Miller indices (hkl) of some strong diffraction peaks are labeled.

Table S8. Fitting result of the XRD pattern of the $Cs_4(Cd_{0.65}Mn_{0.35})Bi_2Cl_{12}$ LDP NCs.

Peak number	Miller indices	2θ (º)	FWHM (º)	*d*-spacing (Å)	Crystallite size (nm)
1	(102)	14.13	1.26	6.268	6.3
2	(110)	23.47	1.02	3.790	8.0
3	(116)	27.61	0.67	3.231	12.3
4	(204)	28.77	0.90	3.103	9.1
5	(208)	33.41	1.01	2.682	8.2
6	(218)	41.23	0.91	2.190	9.3
7	(220)	48.01	0.86	1.895	10.1
8	(318)	54.09	0.59	1.696	15.1

Lattice parameter: $a = 7.578 \pm 0.0004$ Å, $c = 37.20 \pm 0.01$ Å, unit cell volume: 1850.1 ± 0.5 Å^3
Average crystallite size: 9.8 ± 2.8 nm

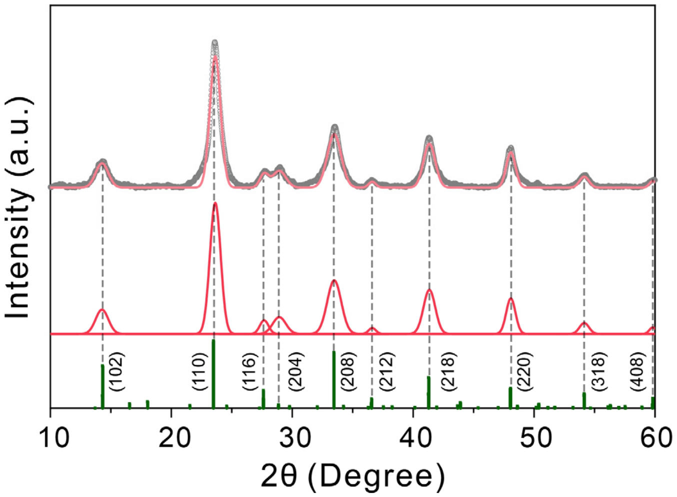

Figure S11. XRD pattern of the $Cs_4(Cd_{0.31}Mn_{0.69})Bi_2Cl_{12}$ LDP NCs. The measured pattern, fitted curves and fitted individual peaks are shown in grey circles, pink lines and red lines, respectively. Calculated diffraction peak positions based on the fitting result are marked in green bars. The Miller indices (hkl) of some strong diffraction peaks are labeled.

Table S9. Fitting result of the XRD pattern of the $Cs_4(Cd_{0.31}Mn_{0.69})Bi_2Cl_{12}$ LDP NCs.

Peak number	Miller indices	2θ (º)	FWHM (º)	*d*-spacing (Å)	Crystallite size (nm)
1	(102)	14.27	1.24	6.209	6.5
2	(110)	23.64	1.04	3.765	7.8
3	(116)	27.68	0.85	3.223	9.6
4	(204)	28.93	1.28	3.087	6.4
5	(208)	33.47	1.36	2.677	6.1
6	(212)	36.62	0.70	2.454	11.9
7	(218)	41.34	1.15	2.184	7.4
8	(220)	48.08	0.90	1.893	9.7
9	(318)	54.15	0.92	1.694	9.7
10	(408)	59.81	0.66	1.546	13.9

Lattice parameter: a = 7.565 ± 0.0004 Å, c = 37.09 ± 0.01 Å, unit cell volume: 1838.3 ± 0.5 $Å^3$
Average crystallite size: 8.9 ± 2.6 nm

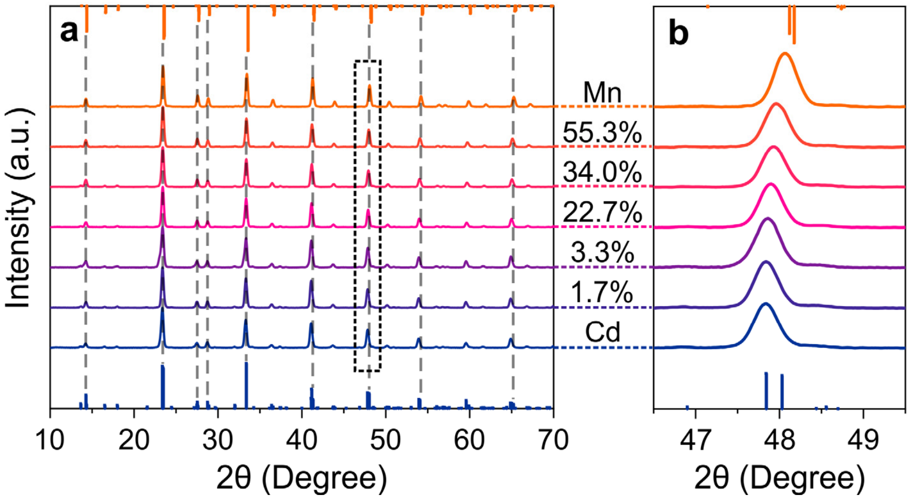

Figure S12. (a) XRD patterns of the $Cs_4(Cd_{1-x}Mn_x)Bi_2Cl_{12}$ LDP powders. **(b)** The zoomed-in area highlighted with a dotted black rectangle in (a).

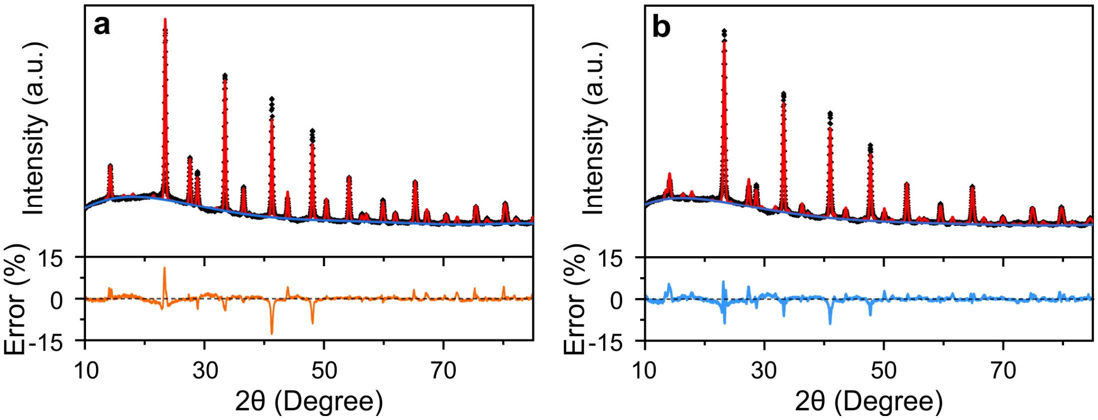

Figure S13. Rietveld fitting of XRD patterns of $Cs_4MnBi_2Cl_{12}$ **(a)**, and $Cs_4CdBi_2Cl_{12}$ **(b)** LDP powders. Experimental, fitting and background curves are marked in black, red and deep blue, respectively. See Table S10-S12 for Rietveld fitting details.

Table S10. Rietveld fitting parameters for $Cs_4MnBi_2Cl_{12}$ and $Cs_4CdBi_2Cl_{12}$ LDP powders

Compound	**$Cs_4MnBi_2Cl_{12}$**	**$Cs_4CdBi_2Cl_{12}$**
Measurement temperature (K)	298	298
Crystal system	Trigonal	Trigonal
Space group	*R*-3*m* (166)	*R*-3*m* (166)
a (Å)	7.570	7.588
c (Å)	37.11	37.24
γ (°)	120	120
Volume (Å^3)	1841	1857
Z	3	3
Density (g/cm^3)	3.869	3.990
Wavelength (Å)	1.541	1.541
Rwp (%)	6.10	5.93
Reflection number	201	201

Table S11. Atomic coordination for $Cs_4MnBi_2Cl_{12}$ by Rietveld fitting

Atom	**Multiplicity**	**x**	**y**	**z**
Bi	6	0.6667	0.3333	0.5858
Cl 1	18	0.3245	0.1623	0.5362
Cl 2	18	0.9710	0.4855	0.6265
Cs 1	6	0.6667	0.3333	0.4616
Cs 2	6	0	0	0.6271
Mn	3	0	0	0.5

Table S12. Atomic coordination for $Cs_4CdBi_2Cl_{12}$ by Rietveld fitting

Atom	**Multiplicity**	**x**	**y**	**z**
Bi	6	0.6667	0.3333	0.5870
Cd	3	0	0	0.5
Cl 1	18	0.2920	0.1460	0.5469
Cl 2	18	0.9710	0.4855	0.6276
Cs 1	6	0.6667	0.3333	0.4609
Cs 2	6	0	0	0.6289

Table S13. ICP-AES-determined Bi, Mn and Cd atomic percentages of $Cs_4M(II)Bi_2Cl_{12}$ LDP powders.

Composition	**Bi (wt. ppm)**	**Mn (wt. ppm)**	**Cd (wt. ppm)**	**(Mn+Cd)/Bi (atom %)**	**Mn/(Mn+Cd) (atom %)**
$Cs_4CdBi_2Cl_{12}$	2.275	0	0.673	55.0	0
$Cs_4(Cd_{0.98}Mn_{0.02})Bi_2Cl_{12}$	13.517	0.031	3.648	51.1	1.7
$Cs_4(Cd_{0.97}Mn_{0.03})Bi_2Cl_{12}$	4.309	0.019	1.140	50.9	3.3
$Cs_4(Cd_{0.87}Mn_{0.23})Bi_2Cl_{12}$	4.241	0.134	0.935	53.0	22.7
$Cs_4(Cd_{0.66}Mn_{0.34})Bi_2Cl_{12}$	5.148	0.242	0.957	52.4	34.0
$Cs_4(Cd_{0.45}Mn_{0.55})Bi_2Cl_{12}$	4.905	0.374	0.618	52.4	55.3
$Cs_4MnBi_2Cl_{12}$	3.814	0.559	0	55.7	100

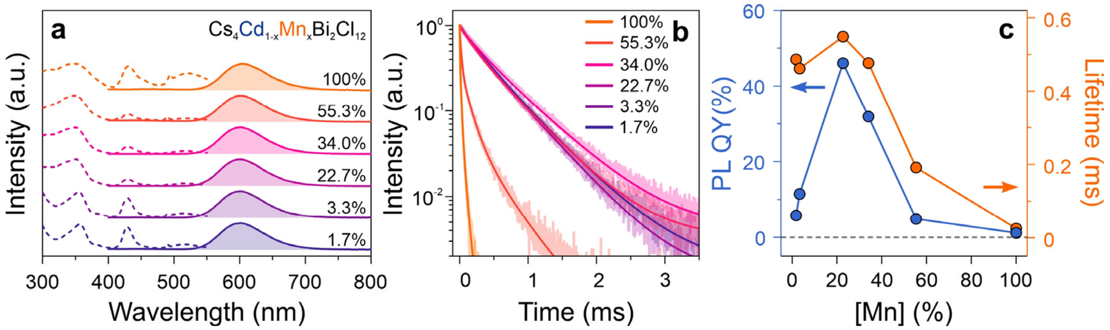

Figure S14. **(a)** PL (solid line) and PLE (dashed line) spectra of the $Cs_4(Cd_{1-x}Mn_x)Bi_2Cl_{12}$ LDP powders. **(b)** TR-PL decay curves of the $Cs_4(Cd_{1-x}Mn_x)Bi_2Cl_{12}$ LDP powders. **(c)** Evolution of PL QY (blue) and average PL lifetime (orange) of the samples as a function of Mn concentration.

Table S14. TR-PL lifetime fitting result of $Cs_4(Cd_{1-x}Mn_x)Bi_2Cl_{12}$ LDP powders

Composition	τ (μs)	Rel. percentage (%)	τ_{avg} (μs)
$Cs_4(Cd_{0.98}Mn_{0.02})Bi_2Cl_{12}$	3.1×10^2	30	4.9×10^2
	5.6×10^2	70	
$Cs_4(Cd_{0.97}Mn_{0.03})Bi_2Cl_{12}$	2.0×10^2	12	4.6×10^2
	5.0×10^2	88	
$Cs_4(Cd_{0.87}Mn_{0.23})Bi_2Cl_{12}$	2.7×10^2	16	5.5×10^2
	6.0×10^2	84	
$Cs_4(Cd_{0.66}Mn_{0.34})Bi_2Cl_{12}$	2.1×10^2	17	4.8×10^2
	5.3×10^2	83	
$Cs_4(Cd_{0.45}Mn_{0.55})Bi_2Cl_{12}$	22	18	1.9×10^2
	1.1×10^2	45	
	3.7×10^2	37	
$Cs_4MnBi_2Cl_{12}$	3.4	15	26
	16	49	
	48	36	

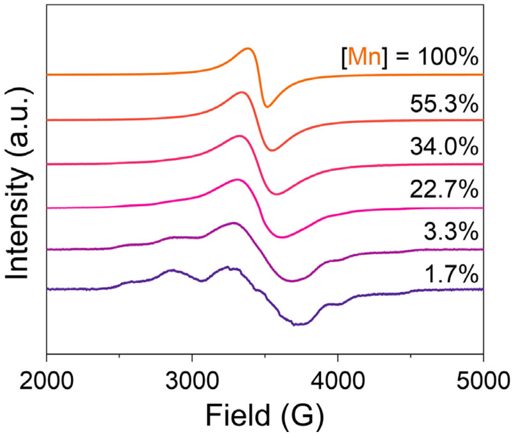

Figure S15. EPR spectra of the $Cs_4(Cd_{1-x}Mn_x)Bi_2Cl_{12}$ LDP powders. [Mn]% = ([Mn]/([Mn] + [Cd])) × 100%.

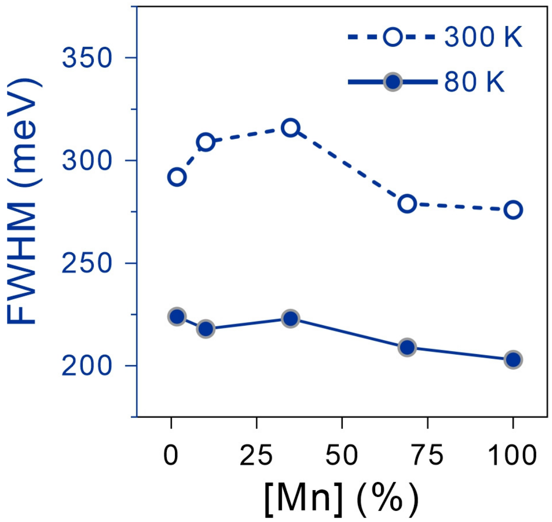

Figure S16. FWHM of the PL profiles of the $Cs_4(Cd_{1-x}Mn_x)Bi_2Cl_{12}$ LDP NCs at low temperature (80 K, solid circle) and room temperature (300 K, open circle) as a function of the Mn concentration.

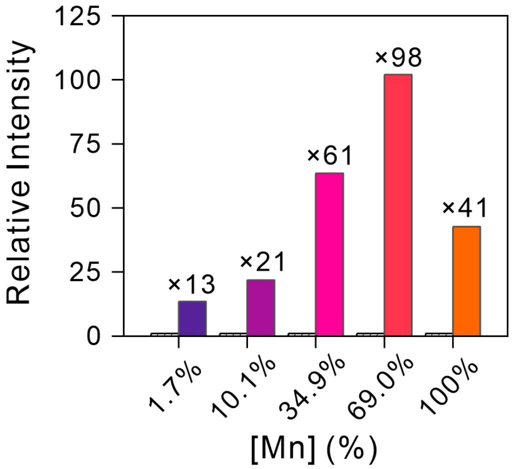

Figure S17. Relative PL intensity of the $Cs_4(Cd_{1-x}Mn_x)Bi_2Cl_{12}$ LDP NCs at low-temperature (80 K) compared with that at room temperature (300 K). The numbers above the colored bars represent the number of folds of PL intensity enhancements.

Table S15. Low temperature TR-PL lifetime fitting results of the $Cs_4(Cd_{1-x}Mn_x)Bi_2Cl_{12}$ LDP NCs.

Composition	**τ (μs)**	**Rel. percentage (%)**	**τ_{avg} (μs)**
$Cs_4(Cd_{0.98}Mn_{0.02})Bi_2Cl_{12}$	3.2×10^2	12	1.2×10^3
	1.3×10^3	88	
$Cs_4(Cd_{0.90}Mn_{0.10})Bi_2Cl_{12}$	3.6×10^2	54	6.6×10^2
	1.0×10^3	46	
$Cs_4(Cd_{0.65}Mn_{0.35})Bi_2Cl_{12}$	4.0×10^2	44	8.6×10^2
	1.2×10^3	56	
$Cs_4(Cd_{0.31}Mn_{0.69})Bi_2Cl_{12}$	4.0×10^2	57	7.1×10^2
	1.4×10^3	43	
$Cs_4MnBi_2Cl_{12}$	1.9×10^2	8.8	8.0×10^2
	5.0×10^2	54	
	1.4×10^3	37	

References

1. M. Imran, V. Caligiuri, M. Wang, L. Goldoni, M. Prato, R. Krahne, L. De Trizio and L. Manna, *J. Am. Chem. Soc.*, 2018, **140**, 2656-2664.
2. B. Vargas, R. Torres-Cadena, J. Rodríguez-Hernández, M. Gembicky, H. Xie, J. Jiménez-Mier, Y.-S. Liu, E. Menéndez-Proupin, K. R. Dunbar, N. Lopez, P. Olalde-Velasco and D. Solis-Ibarra, *Chem. Mater.*, 2018, **30**, 5315-5321.
3. T. J. B. Holland and S. A. T. Redfern, *Mineral. Mag.*, 1997, **61**, 65-77.
4. G. Kresse and D. Joubert, *Phys. Rev. B*, 1999, **59**, 1758-1775.
5. G. Kresse and J. Furthmüller, *Phys. Rev. B*, 1996, **54**, 11169-11186.
6. P. E. Blöchl, *Phys. Rev. B*, 1994, **50**, 17953-17979.
7. J. P. Perdew, K. Burke and M. Ernzerhof, *Phys. Rev. Lett.*, 1996, **77**, 3865.
8. J. Heyd, G. E. Scuseria and M. Ernzerhof, *J. Chem. Phys.*, 2003, **118**, 8207-8215.
9. B. Vargas, R. l. Torres-Cadena, J. Rodriguez-Hernandez, M. Gembicky, H. Xie, J. Jiménez-Mier, Y.-S. Liu, E. Menéndez-Proupin, K. R. Dunbar and N. Lopez, *Chem. Mater.*, 2018, **30**, 5315-5321.
10. A. D. Becke and K. E. Edgecombe, *J. Chem. Phys.*, 1990, **92**, 5397-5403.
11. A. Savin, R. Nesper, S. Wengert and T. F. Fässler, *Angew. Chem. Int. Ed.*, 1997, **36**, 1808-1832.
12. P. De Silva, J. Korchowiec and T. A. Wesolowski, *ChemPhysChem*, 2012, **13**, 3462-3465.
13. N. P. Holzapfel, J. D. Majher, T. A. Strom, C. E. Moore and P. M. Woodward, *Chem. Mater.*, 2020, **32**, 3510–3516.
14. S. W. S. McKeever, B. Jassemnejad, J. F. Landreth and M. D. Brown, *J. Appl. Phys.*, 1986, **60**, 1124-1130.
15. W. Lee, D. Choi and S. Kim, *Chem. Mater.*, 2020, **32**, 6864-6874.
16. S. B. Oseroff, *Phys. Rev. B*, 1982, **25**, 6584-6594.
17. P. H. Borse, D. Srinivas, R. F. Shinde, S. K. Date, W. Vogel and S. K. Kulkarni, *Phys. Rev. B*, 1999, **60**, 8659-8664.
18. V. Di Castro and G. Polzonetti, *J. Electron. Spectrosc. Relat. Phenom.*, 1989, **48**, 117-123.